Heliyon 9 (2023) e22001

Contents lists available at ScienceDirect

Heliyon

journal homepage: www.cell.com/heliyon

Ultrasound-assisted adsorption of organic dyes in real water samples using zirconium (IV)-based metal-organic frameworks UiO-66-NH_2 as an adsorbent

Abdeslam Assafi [a], Youssef Aoulad El Hadj Ali [a], Rasmiah S. Almufarij [b], Lamia Hejji [a,c], Nadeem Raza [d,*], Luis Pérez Villarejo [c], Badredine Souhail [a], Abdelmonaim Azzouz [a,**], Ehab A. Abdelrahman [d,e]

[a] Department of Chemistry, Faculty of Science, University of Abdelmalek Essaadi, B.P. 2121, M'Hannech II, 93002, Tetouan, Morocco
[b] Department of Chemistry, College of Science, Princess Nourah Bint Abdulrahman University, P.O. Box 84428, Riyadh, 11671, Saudi Arabia
[c] Department of Chemical, Environmental, and Materials Engineering, Higher Polytechnic School of Linares, University of Jaén, Campus Científico-Tecnológico, Cinturón Sur s/n, 23700, Linares, Jaén, Spain
[d] Department of Chemistry, College of Science, Imam Mohammad Ibn Saud Islamic University (IMSIU), Riyadh, 11623, Saudi Arabia
[e] Chemistry Department, Faculty of Science, Benha University, Benha, 13518, Egypt

ARTICLE INFO

Keywords:
Ultrasound assisted adsorption
Metal-organic frameworks
Adsorption kinetics
UiO-66-NH_2
Dyes pollutants
Environmental safety

ABSTRACT

The utilization of dye adsorption through metal-organic frameworks represents an eco-friendly and highly effective approach in real water treatment. Here, ultrasound assisted adsorption approach was employed for the remediation of three dyes including methylene blue (MB), malachite green (MG), and congo red (CR) from real water samples using zirconium(IV)-based adsorbent (UiO-66-NH_2). The adsorbent was characterized for structural, elemental, thermal and morphological features through XRD, XPS, FTIR, thermogravimetric analysis, SEM, BET , and Raman spectroscopy. The adsorption capacity of adsorbent to uptake the pollutants in aqueous solutions was investigated under different experimental conditions such as amount of UiO-66-NH_2 at various contact durations, temperatures, pH levels, and initial dye loading amounts. The maximum removal of dyes under optimal conditions was found to be 938, 587, and 623 mg g^{-1} towardMB, MG, and CR, respectively. The adsorption of the studied dyes on the adsorbent surface was found to be a monolayer and endothermic process. The probable mechanism for the adsorption was chemisorption and follows pseudo-second-order kinetics. From the findings of regeneration studies, it was deduced that the adsorbent can be effectively used for three consecutive cycles without any momentous loss in its adsorption efficacy. Furthermore, UiO-66-NH_2 with ultrasound-assisted adsorption might help to safeguard the environment and to develop new strategies for sustainability of natural resources.

1. Introduction

According to a latest report of World Health Organization (WHO), nearly 844 million individuals globally have nonaccess to safe

* Corresponding author
** Corresponding author
E-mail addresses: nadeemr890@gmail.com, nrmostafa@imamu.edu.sa (N. Raza), aazzouz@uae.ac.ma (A. Azzouz).

https://doi.org/10.1016/j.heliyon.2023.e22001
Received 15 June 2023; Received in revised form 27 October 2023; Accepted 1 November 2023
Available online 8 November 2023

drinking water [1]. As a consequence of industrialization and urbanization, it is anticipated that in the near future, clean and potable water will become scarcer and more costly due to pollution [2]. The textile industry has emerged as the main contributor to water pollution among the different sources, primarily due to the frequent discharge of untreated effluent contaminated with dyes into natural aquatic environments [2–4]. The dyes are widely employed in the manufacture of various consumer goods, including painting, printing, paper, tanning, plastics, textiles, coatings, rubber, and so on [5,6]. Currently, it has been calculated that the textile industry produces around 7.0×10^5 tons of organic dyes annually, making them as major pollutants [7,8]. Methylene blue (MB), malachite green (MG), and congo red (CR) collectively comprise a substantial portion of this organic dyes manufactured and utilized annually, and they are substances that pose significant health hazards. MG is known for its potential teratogenic and carcinogenic properties, which can lead to damage in vital organs like the liver, kidney, and heart. Additionally, it can cause skin, lung, and bone lesions [9]. MB, on the other hand, is toxic, carcinogenic, and non-biodegradable, and its decomposition generates harmful compounds (such as sulfur oxides, nitrogen oxides, and carbon monoxide), which are closely associated with severe illnesses such as cancer, gastritis, and hypertension [10,11]. CR is classified as an anion diazo dye and is one of the most commonly used dyes [12]. Unfortunately, under anaerobic conditions CR degradation leads to the production of benzidine, a well-recognized human carcinogen, that for the human health side, for the environmental side the prevalence of CR dye-containing wastewater, particularly from industries such as printing and dyeing, exerts detrimental impacts on the ecological system [13]. Hence, it is crucial to confiscate organic dyes pollutants from environmental water resources to mitigate their harmful effects on humans, flora, and fauna.

In this concern, diverse approaches have been used for removal of dyes from environmental water resources include advanced oxidation system [14,15], photocatalysis [16–19], electrocoagulation [20], Fenton oxidation [21,22], electrokinetic remediation [23,24], ultrasonication [6], membrane bioreactor [4,25], and multifunctional materials for thermal degradation [26]. These approaches are linked with several other disadvantages such as high installation and operational cost, complex chemistry, large requirements of oxidant, time consuming process, and oxidant handling problems [27]. However, adsorption process is considered as one of the most efficient alternative approaches for dyes removal from water [3,8,28–33], due to its simplicity, low cost, high treatment effectiveness, high potential, less energy consumption, and easy operation [5,27]. For these reasons, many recent studies have employed adsorption as a prominent technique to eliminate diverse dye pollutants from diverse environmental water. For example, El-Nemr et al. conducted an exemplary adsorption experiment aimed at the elimination of Acid Yellow 36 dye [34]. Furthermore, Mujtaba et al. achieved notable success in the elimination of MB dye through the utilization of adsorption [35]. Additionally, Eltaweil et al. executed a highly effective elimination process targeting MG dye, employing the adsorption method [9]. Among diverse adsorbents zeolites [36], graphene oxide-based nanocomposites [37], and metal organic frameworks (MOFs) have been substantially deployed to remove dyes pollutants from water-based matrices [29–32].

The intrinsic characteristics of MOFs, such as extensive surface area, substantial porosity, and adjustable structure make them a promising alternative to conventional materials for diverse applications including photocatalysis, energy storage, catalysis, drug delivery, sensing applications, liquid and gas phase adsorption [38]. The pore size variability of MOFs enables them to adsorb a broad range of organic and inorganic compounds [39]. Among several kinds of MOFs zeolitic imidazolate framework 8 (ZIF-8), HKUST-1, MIL-101, MIL-53, Zn-MOF, and UiO-66 have been applied in adsorption of dyes [40,41]. For instance, the ZIF-8 as an adsorbent exhibited remarkable calculated adsorption capacity (1667 mg g^{-1}) relative to activated carbon (200 mg g^{-1}) to remove MG dye [42]. Additionally, MOF-1 nanocomposite was successfully used in removing CR dye from water and showcased an adsorption capacity around 104 mg g^{-1} [43]. Whereas MIL-100(Fe) was found to have an ultra-high adsorption capacity (1019 mg g^{-1}) for MB dye [44]. Furthermore, UiO-66-NH_2 has been studied as a promising nanomaterials for water treatment and dye removal owing to its outstanding chemical, structural, and thermal stability, which is attributed to the presence of Zr–O bonds linked by dicarboxylate ligands [45,46]. For example, Ahmadijokani et al. reported relatively low adsorption capabilities for the investigated dyes including MG (133 mg g^{-1}) and MB (370 mg g^{-1}) using UiO-66-NH_2 [47]. In another study, during the CR removal by UiO-66-NH_2, significantly less adsorption capacity of 94.2 g mg^{-1} was obtained [46]. To this end, it is highly desirable to significantly improve the adsorption capacity of target dyes using UiO-66-NH_2 framework through some effective strategies.

The present study focuses to meticulously investigate the adsorption of three dyes including MG, MB, and CR in real water samples using UiO-66-NH_2 nanocomposites-based ultrasound-assisted adsorption. In the following, the effect of ultrasound radiation on the amount of the adsorbed organic dyes has been investigated. The adsorption capacity and rate constants were analyzed through adsorption isotherms and kinetics. The impact of various factors, including initial dye loading levels, contact durations, solution pH-level, co-existing salts, amount of adsorbent, and temperature impact on dyes adsorption were explored. The findings demonstrated excellent adsorption capacity under optimized experimental conditions. The mechanism of adsorption process was explored based on the pH effect and Fourier transform infrared (FTIR) spectra obtained pre- and post-adsorption. In addition, the stability of UiO-66-NH_2 was evaluated to determine its suitability for long-term applications. On one hand, it is imperative to highlight the innovation inherent in our developed approach, which centers on harnessing ultrasound waves to enhance the adsorption process significantly. This augmentation notably boosts the adsorbent's capacity, resulting in a significant enhancement of adsorption efficiency. Consequently, the incorporation of ultrasound not only enhances efficacy but also reduces procedural costs and confers excellent commercial viability, rendering it applicable on a large scale. On the other hand, the proposed approach based on UiO-66-NH_2 nanocomposite – assisted ultrasound irradiation provided outstanding features, such as simple synthesis, structural stability, cost-effectiveness (reusability for three cycles), lack of production of secondary pollution, and effectiveness in real water samples including river, dam, and wastewater.

2. Experimental

2.1. Reagents

Zirconium(IV) oxychloride octahydrate ($ZrOCl_2{\cdot}8H_2O$, 98 %), 2-amino-terephthalic acid ($C_8H_7O_4N$, 99 %), N,N-dimethylformamide (DMF) (C_3H_7ON, 99.9 %), sodium hydroxide (NaOH, 98 %), and ethanol (C_2H_6O, 99.8 %) were obtained from Sigma Aldrich (Germany). CR dye ($C_{32}H_{22}N_6Na_2O_6S_2$), hydrochloric acid (HCl, 37 %) was purchased from Lobachemie. MG ($C_{23}H_{25}ClN_2$, 99 %) and MB ($C_{16}H_{24}ClN_3O_3S$, 95.1 %) were obtained from Acros Organics.

2.2. Synthesis of UiO-66-NH_2

The UiO-66-NH_2 nanocomposites were fabricated by modifying the previous protocol [48]. Briefly, 395 mg of $ZrOCl_2{\cdot}8H_2O$ were dissolved into a solution of 5 mL DMF, and 3 mL of 37 % HCl were introduced to mixture. To ensure the proper mixing, above mixture was stirred for 1 h at room temperature, and then sonicated for 30 min. Afterwards, 388 mg of 2 amino-terephthalic acid were solubilized in 31.54 mL of DMF and mixed into the first solution. The resultant mixture underwent a 30 min sonication process before heating in an oven at 80 °C for 12 h. The mixture was filtered and the solid crystals were washed with DMF and ethanol and were dispersed in 10 mL of ethanol. After 24 h, the mixture was sieved to obtain the solid crystals which were subjected to three wash cycles to ensure the elimination of solvent contaminants. Finally, the UiO-66-NH_2 was subjected to a 12 h drying process at 90 °C in an oven.

2.3. Equipment and apparatus

Surface chemical composition of UiO-66-NH_2 and functionalization of the tested adsorbents were confirmed by Vertex 70 Bruker equipment of Attenuated Total Reflectance FTIR spectroscopy scanned from 4000 to 400 cm^{-1}. X-ray diffraction (XRD) patterns of UiO-66-NH_2 were obtained using Bruker diffractometer (Phillips Xpert-pro model, using Cu Kα $\lambda = 1.54051$ Å radiation with a step of 0.017°/1 s) to determine the crystallin phase. The Raman spectra were recorded with an Oriba Raman spectroscopy using 532.28 nm (green) laser excitation. Acquisition time spanned from 10 to 20 s during five cycles to determine the chemical structure and the disorder of the as prepared materiel. The morphology features of the UiO-66-NH_2 were obtained by Scanning Electron Microscopy (SEM) (Zeiss Sigma 500 VP Analytical FE-SEM, Inspect Carl Zeiss Company, Germany) using a JEOL model SM 840 with Energy Dispersive X-ray spectroscopy (EDX). The precursors were placed on an aluminum grid to coat with carbon using a JEOL JFC 1100 sputter coater. The surface chemical states and the quantitative analysis have been investigated by X-ray photoelectron spectroscopy (XPS) analysis (Physical Electronics VersaProbe II Scanning XPS photoelectron spectrometer equipped with a monochromatic X-ray Al Kα radiation source). Thermogravimetric analysis (TGA) was achieved using SDT Q600 Auto-DSCQ20 system to determine the thermal stabilities of the UiO-66-NH_2. For this characteristic, the UiO-66-NH_2 samples kept in an alumina pan were heated from 20 to 800 °C at a ramping rate of 10 °C min^{-1} with N_2 supplied at a rate of 100 mL min^{-1}. The specific surface area of the adsorbents was determined using Brunauer–Emmett–Teller (BET) (Micromeritics equipment, TriStar II 3020 model), following the BJH method at -196 °C.

2.4. Batch experiments

The capacity of UiO-66-NH_2 to adsorb MG, CR, and MB was investigated through a sequence of batch experiments. In each adsorption experiment certain amount of UiO-66-NH_2 was inserted into 100 mL of dye solution in the presence of ultrasonic waves (ULTASOUNS-H J.P. SELECTA, Hz: 50/60, W: 720) to ensure the adsorption equilibrium. Afterwards, the solution was centrifuged (11000 rpm, 5min) and its absorbance was measured employing a UV/visible spectrophotometer (HACH LANGE GmbH DR 2800). The quantity of dye adsorbed on the surface of adsorbent at equilibrium (Q_e, mg g^{-1}) and the percentage of dye elimination (E %) were calculated using equations (1) and (2) [49].

$$Q_e = \frac{(C_i - C_e)V}{m} \tag{1}$$

$$E(\%) = \frac{(C_i - C_e)}{Ci} \times 100 \tag{2}$$

Q_e: quantity of dye adsorbed on the surface of UiO-66-NH_2 (mg g^{-1}), C_i: initial concentration of dye (mg L^{-1}), C_e: concentration of dye at equilibrium (mg L^{-1}), V is the solution volume (L), m is the mass of the adsorbent (g). Many factors (such as adsorbent dose, contact time, pH of solution, initial dye concentration, ionic strength, and temperature of reaction medium) that can affect the adsorption of dyes on the adsorbent surface were evaluated through triplicate experiments.

2.5. Adsorption kinetics

In general, the analysis of adsorption kinetics is employed to clarify the adsorption mechanism, that involves the mass transfer, diffusion, and reactions occurring on the adsorbent surface along with its rate. The most typical kinetic models used to keep track of the adsorption kinetics are Lagergren's pseudo-first-order model (PFO) and Ho's pseudo-second-order model (PSO) [50]. In this work, the kinetics of dyes adsorption onto UiO-66-NH_2 was investigated using a batch equilibrium system with contact time ranging from 5 to

210 min, and initial dye concentration from 10 to 200 mg L^{-1}.

According to PFO model, the speed of the adsorption process is controlled by variation in the quantity of molecules adsorbed onto the adsorbent surface during the period from the equilibrium adsorption time to a predetermined moment, which generally indicates that physisorption controls the adsorption phenomenon [51]. The following presentation (equation (3)) elucidates the sophisticated mathematical representation associated with this model:

$$Q_t = Q_e\left(1 - e^{k_1 t}\right) \tag{3}$$

Q_t: the quantity of dye adsorbed on UiO-66-NH_2 (mg g^{-1}) at time t (min), Qe: the quantity of dye adsorbed on UiO-66-NH_2 (mg g^{-1}) at equilibrium time, k_1: is rate constant of PFO kinetic model (min^{-1}).

According to the PSO model, it is suggested that chemisorption controls the adsorption process in which sharing of electrons between an adsorbate and an adsorbent is considered as a rate-limiting step. The mathematical representation of this model is described below (equation (4)):

$$Q_t = \frac{Q_e^{\,2} k_2 t}{1 + Q_e k_2 t} \tag{4}$$

Q_t: the quantity of dye adsorbed on UiO-66-NH_2 (mg g^{-1}) at time t (min), Q_e: the quantity of dye adsorbed on UiO-66-NH_2 (mg g^{-1})

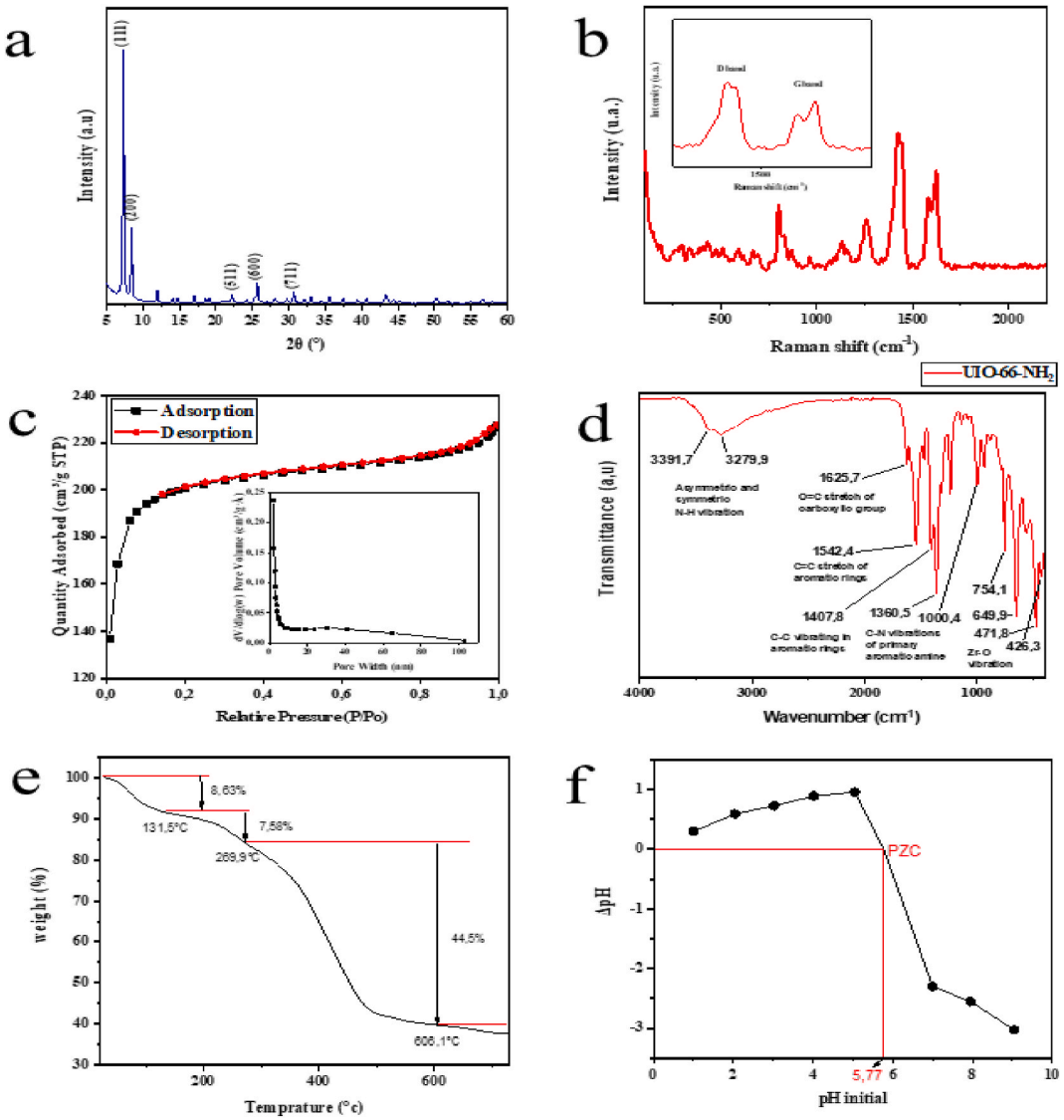

Fig. 1. Structural characterization of UiO-66-NH_2: (a) XRD, (b) Raman, (c) N_2 curve, and porosity distribution, (d) FTIR spectra, (e) TGA curve, and (f) pH value correspondent to the neutral surface charge.

at equilibrium time, k_2: is the rate constant of the PSO kinetic model (g mg^{-1} min^{-1}).

2.6. Adsorption isotherms

In order to evaluate the nature of adsorption of dyes on adsorbent surface, it is highly desirable to evaluate isotherm data. In this work two isotherm models (Langmuir and Freundlich) have been applied for the evaluation of data.

- **Langmuir isotherm**

The Langmuir model presumes that no chemical interactions occur between adsorbate and adsorbent molecules and a homogeneous monolayer adsorption takes place on the surface of employed adsorbent [49]. The quantity of dye adsorbed and separation factor can be expressed as follows:

$$Q_e = \frac{Q_m k_L C_e}{1 + k_L C_e} \tag{5}$$

$$R_L = \frac{1}{1 + k_L C_0} \tag{6}$$

Q_e: the adsorption capacity of dye (mg g^{-1}), Q_m: the maximum capacity in monolayer saturation determined by the theoretical Langmuir model (mg g^{-1}), K_L: the Langmuir equilibrium constant (L mg^{-1}), C_e: the dye concentration at equilibrium (mg L^{-1}), C_0: initial dye concentration (mg L^{-1}), R_L: separation factor.

- **Freundlich isotherm**

According to the concept of Freundlich isotherm model adsorption process occurs through a multi-layered pattern on heterogeneous surfaces of adsorbent. In this way, the model describes the various characteristics of the adsorption process such as the continuous increase in the adsorbed amount with increasing concentration [52]. According to this model, the quantity of dye adsorbed can be expressed as following:

$$Q_e = K_F C_e^{1/n} \tag{7}$$

Q_e: the adsorption capacity of dye (mg g^{-1}), C_e: the dye concentration remaining in solution at equilibrium (mg L^{-1}), K_F: the Freundlich constant, n: the heterogeneity factor indicating the adsorption intensity.

3. Results and discussion

3.1. Characterization of UiO-66-NH_2

In order to obtain XRD patterns of UiO-66-NH_2, XRD was employed and the patterns are depicted in Fig. 1a, which illustrates the existence of characteristic peaks at 7.42, 8.59, 22.28, 25.78 and 30.78° and confirms the synthesis of UiO-66-NH_2 [53,54]. The narrow lines of the XRD pattern indicate the high crystallinity of adsorbent and also are in good agreement with the literature about the characteristics of this materiel [53–55].

The Raman spectra of UiO-66-NH_2 Fig. 1b indicated the successful synthesis of the nano material which was similar to other studies reported in literature [56,57]. The D band (also known as the disorder or defect band) related to the presence of defects or disorder in the material and the G band corresponds to the first-order scattering of the E2g phonon mode, which is related to the sp2 hybridization of carbon atoms were detected respectively at 1434 cm^{-1} and 1597 cm^{-1}.

The BET analysis of UiO-66-NH_2 (Fig. 1c) revealed a type I isotherm, which exhibits a steep rise in the adsorption curve at low relative pressures and a plateau region, indicating that the material has a highly porous structure with well-defined micropores (pore size of 2.0 nm). Furthermore, the analysis showed that BET surface area of adsorbent is 679 m^2 g^{-1}, and the Langmuir surface area of the material is even higher at 902 m^2 g^{-1} which represents the maximum monolayer coverage of adsorbed molecules on the surface of the material. The Barrett-Joyner-Halenda (BJH) method was deployed to find the cumulative surface area and cumulative volume of pores which were 75 m^2 g^{-1} and 0.075 cm^3 g^{-1}, respectively (**Table 1**).

The presence of the functional groups in the UiO-66-NH_2 was identified using the FTIR. In Fig. 1d (FTIR spectra of UiO-66-NH_2), the two absorption peaks appeared at 3391.7 and 3279.9 cm^{-1} were assigned to the symmetric and asymmetric vibrations of NH_2 (each N–H) group respectively [58]. The peaks at 1542.4 cm^{-1} and 1407.8 cm^{-1} were ascribed to C═C stretching and C–C vibration of

Table 1
The BET and BJH data of UiO-66-NH_2.

Sample	S_{BET} (m^2g^{-1})	$S_{Langmuir}$ (m^2 g^{-1})	Pore size (nm)	Cumulative surface area of pores (BJH) (m^2 g^{-1})	Cumulative volume of pores (BJH) (cm^3 g^{-1})
UiO-66-NH_2	679	902	2.0	75	0.075

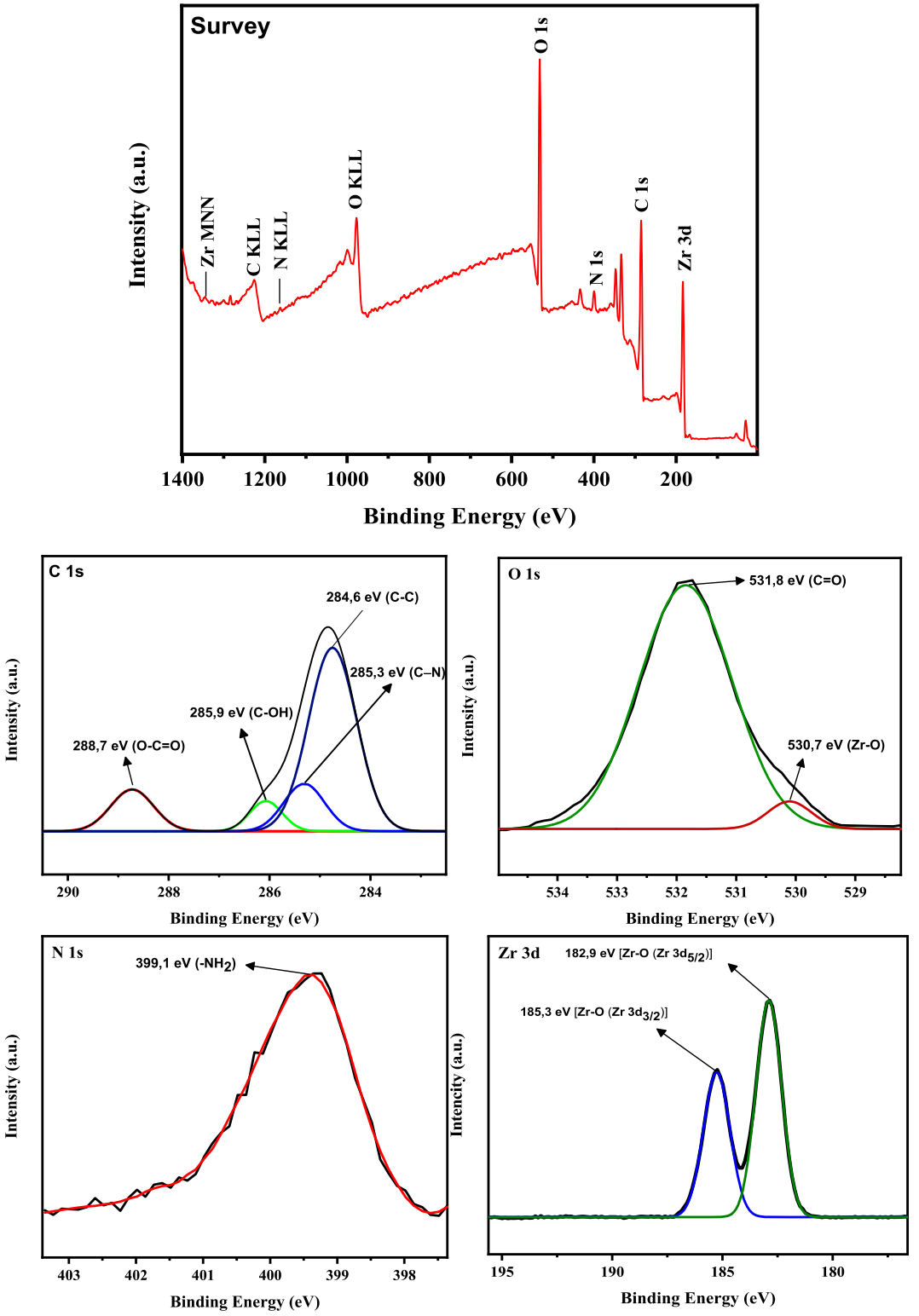

Fig. 2. XPS spectra of UiO-66-NH_2 (Survey, C 1s, O 1s, N 1s and Zr 3d regions).

aromatic rings from 2-amino-terephthalic acid, respectively [59]. In addition, the peak at 1625.7 cm^{-1} was the characteristic of C═O vibration of carboxyl group present in 2-amino-terephthalic acid groups in UiO-66-NH_2 [60]. The moderate peak at 1000.4 cm^{-1} and the strong one at 1360.5 were attributed to C–N bonds between aromatic carbon and nitrogen [60]. However, the observed peaks in the range of 800–600 cm^{-1} were ascribed to the vibration of Zr–O (Zr metal and the oxygen molecule of carboxyl group in 2-amino-terephthalic acid) [61].

The morphological characteristics of UiO-66-NH_2 are shown in Fig. 1S which demonstrates the presence of agglomerated spherical particles with size in the range of 111.9–260.1 nm.

The TGA curve of UiO-66-NH_2 (Fig. 1e) indicates an 8.63 % loss of weight from 20 to 103.5 °C is due to moisture contents in the sample. Whereas, weight loss of 7.58 % between 131.1 and 269.9 °C is due to the degradation of DMF physiosorbed into the adsorbent. Significant weight reduction amounting to 44.5 % was observed within the temperature range spanning from 269.9 °C to 606.1 °C is related to the degradation of organic ligand (2-amino-terephthalic acid) [62].

The identification of elements and determination of binding energies among individual elements present in the synthesized nanomaterial (UiO-66-NH_2) was executed by XPS and the results are shown in Fig. 2 which confirms the electronic and chemical states of the elements present in UiO-66-NH_2.

The XPS spectra derived from the analysis of UiO-66-NH_2 (Fig. 2) shows the presence of C, O, N, and Zr with different percentages (Table 1S). The C 1*s* spectrum consisting of 4 contributions at 288.7, 285.9, 285.3, and 284.6 eV can be attributed to the presence of O–C═O, C-OH═, C–N, and C–C/-C=C-/adventitious carbon present in 2-amino terephthalic acid. The N 1*s* spectrum shows one peak at 399.1 eV that confirms the existence of –NH_2 group of 2-amino terephthalic acid (not linked with Zr metal). The O 1*s* spectrum consists of two peaks at 531.8 and 530.7 eV correspond to C═O group and to the liaison between the oxygen from 2-amino terephthalic acid and Zr metal. Finally, Zr 3d pattern confirms the liaison between 2-amino terephthalic acid and Zr metal by showing tow peaks at 182.3 and 182.9 eV due to the interaction between Zr metal and oxygen of 2-amino terephthalic acid.

3.2. Studies of adsorption parameters

3.2.1. Effect of adsorbent amount

The adsorbent dose is a crucial factor which benefits to determine the ideal amount of adsorbent that gives the maximum adsorption of an analyte. The effect of UiO-66-NH_2 dose was examined by varying its amount from 0.5 to 7.5 mg in 100 mL of known dye (MG, CR, and MB) concentration (10 mg L^{-1}). The results shown in Fig. 3 illustrate that the adsorbed amount of dye gradually

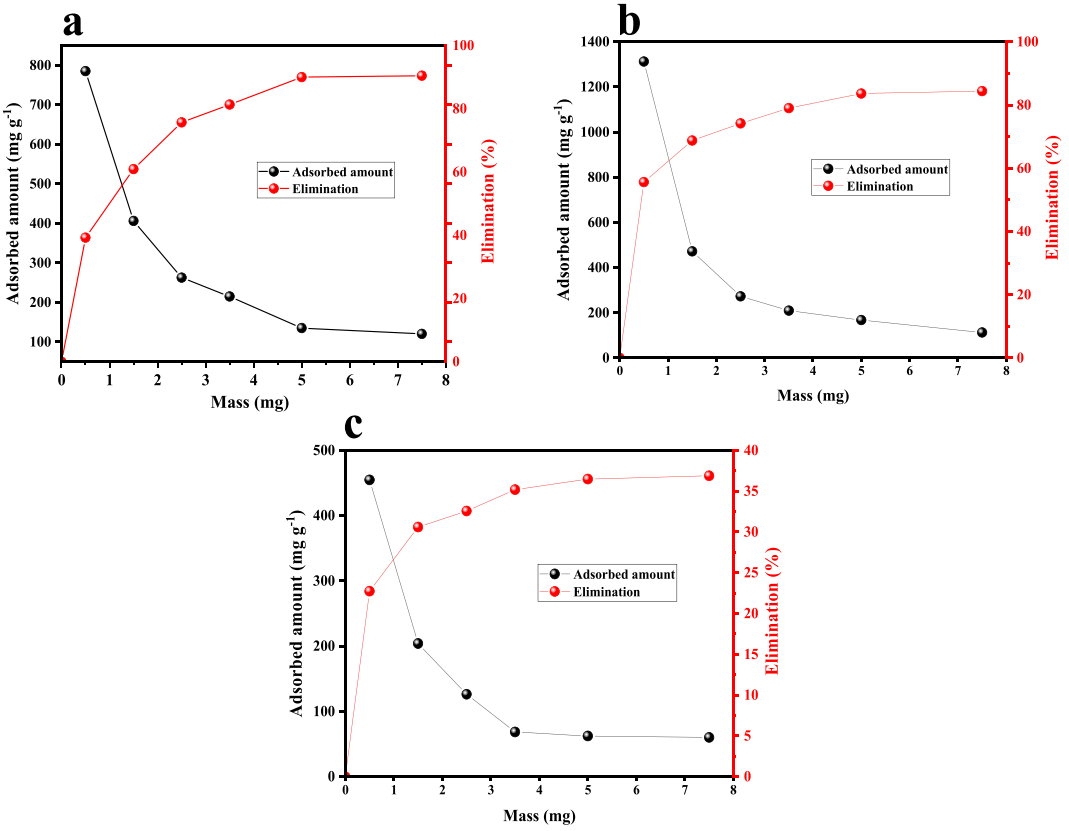

Fig. 3. Effect of adsorbent dose on CR (a), MB (b), and MG (c) adsorption.

raised with an increase in adsorbent mass until the saturation point. The optimal mass was found to be 5 mg for all the used dyes (for CR Fig. 3a: $Q_e = 135$ mg g^{-1}; E% = 90 % at t = 291.15 K, $pH_i = 5$, for MB Fig. 3b: $Q_e = 163$ mg g^{-1}; E% = 83.63 % at t = 291.15 K, pH_i = 6,15, and for MG Fig. 3c: $Q_e = 62.2$ mg g^{-1}; E% = 36.5 % at t = 291.15 K, $pH_i = 5$).

3.2.2. Effect of contact time

The impact of contact durations is generally used to assess the adsorption ability of the nanomaterial for a typical target. To explore the impact of contact duration on the efficacy of UiO-66-NH_2 in removing dye pollutants, 5 mg of the nanomaterial was added in 100 mL of dye solution under ultrasonic waves. The results of the study (Fig. 4 a-c) reveals that an increase in contact time causes a significant rise in adsorbed amount of target dye until equilibrium (around 60 min). Fig. 4 (a-c) also indicates that 0–30 min contact time, the adsorption of dyes occurs quickly and after 30 min continues steadily until equilibrium is achieved. The substantial surface area and the plethora of active sites were likely responsible to this phenomenon in the initial phase, and where the adsorption reaction becomes slow in the second phase, may be due to the growing saturation on the adsorbent surface which prevents the non-adsorbed dye molecules to get adsorbed [63].

3.2.3. Effect of amount of dye

Initial dye loading levels exerts a significant influence in the activation of the adsorption system. Herein, the varying levels of dye concentration (from 10 to 200 mg L^{-1}) were used to achieve the best possible results. 5 mg of adsorbent-nanomaterial was mixed into 100 mL of each initial dye concentration under ultrasonic waves and ambient conditions. Fig. 2S shows that an elevation in the initial concentration of the target dye significantly increases the adsorption capability. As shown in Fig. 2S, for the MB and CR, it is evident that the concentration of 10 mg L^{-1} resulted into maximum elimination efficiency with UiO-66-NH_2, after that further rise in the initial dye amount i.e., greater than 20 mg L^{-1}) results in significant reduction in its removal rate. But for MG at the first, the rise in the initial concentration from 10 to 20 mg L^{-1} causes a significant increase in the removal efficiency however, the reverse trend in adsorption of MG occurs as its concentrations is further increased from 30 mg L^{-1}.

3.2.4. Effect of pH

The pH-level impact in dyes adsorption study is considered as crucial factor as it can affect both the adsorbent structure and adsorption mechanism and leads to variation in the retention efficiency. In this experiment, the efficiency of adsorption of CR, MB, and

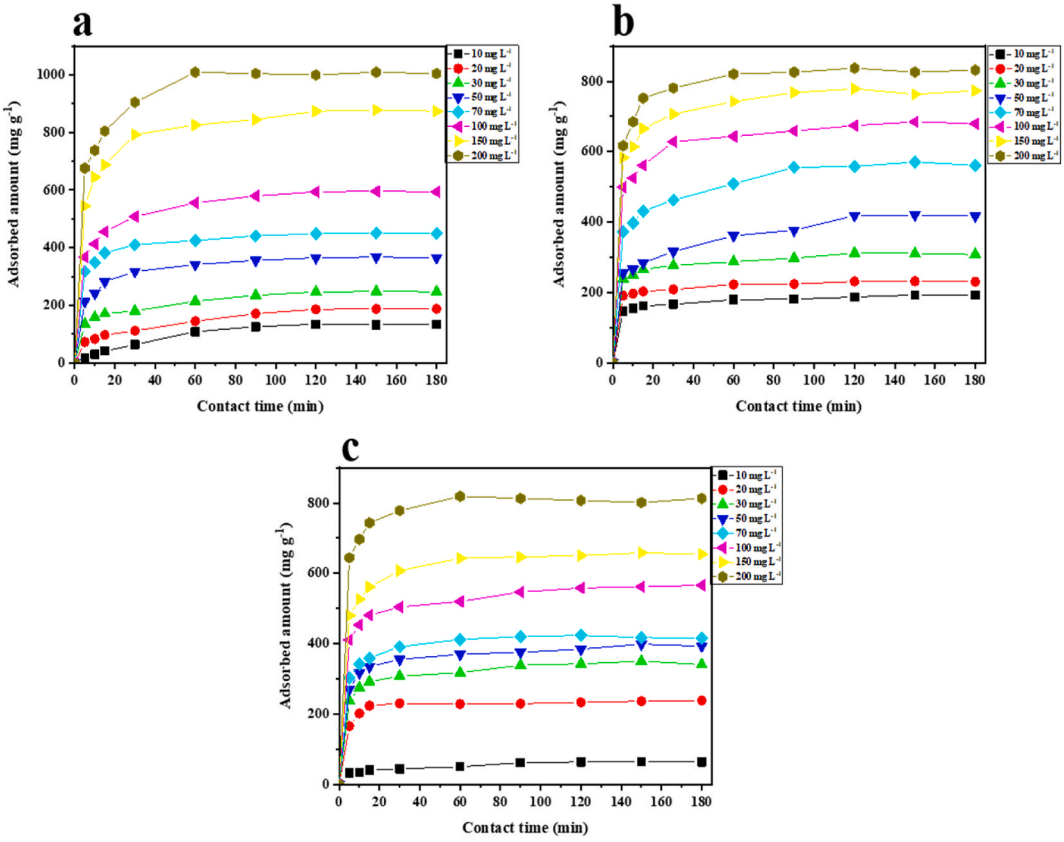

Fig. 4. Effect of contact time and initial CR (a), MB (b), and MG (c) concentration.

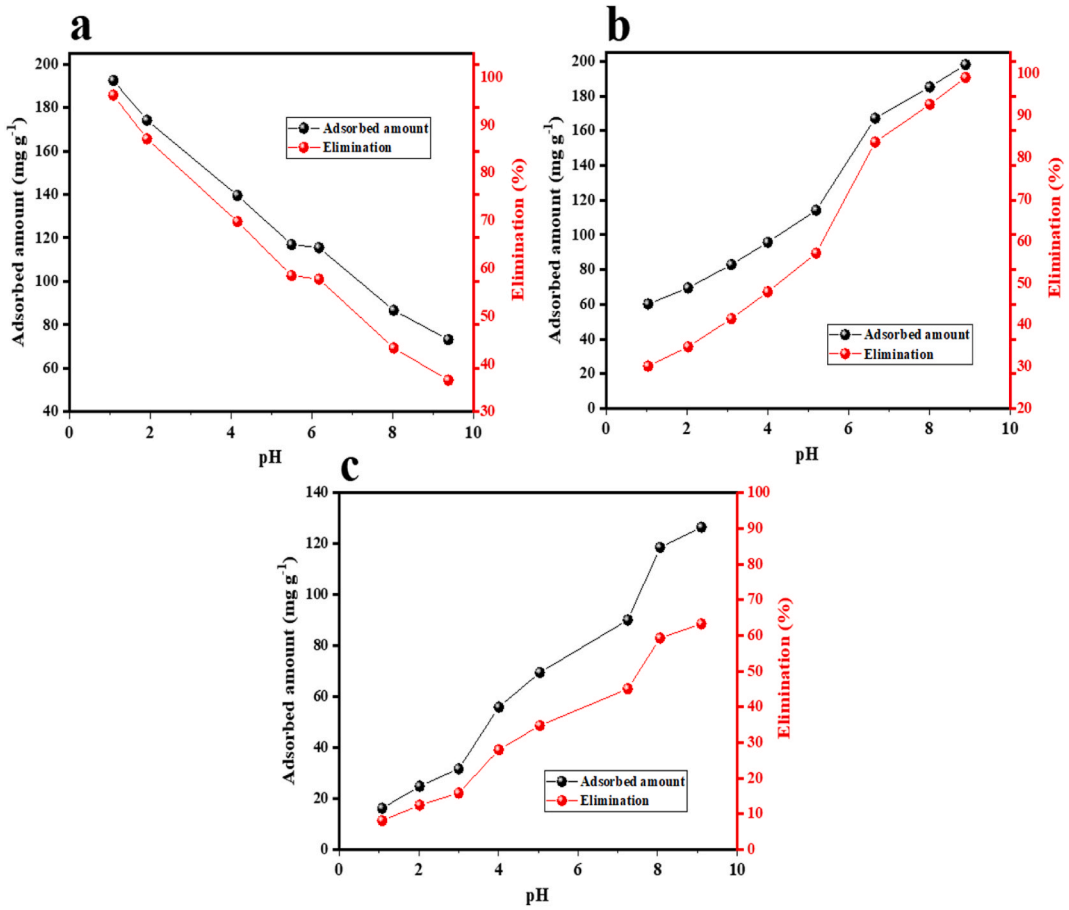

Fig. 5. Effect of pH on the sorption of CR (a), MB (b), and MG (c) onto UiO-66-NH_2 nanocomposite.

MG was scrutinized by adjusting the initial pH from 1 to 9 using HCl (0.1 mol L^{-1}) and NaOH (0.1 mol L^{-1}) in 100 mL of 10 mg L^{-1} of dye solutions containing 5 mg of adsorbent under ultrasound waves and equilibrium time of 60 min. From Fig. 5(a–c), it is clear that the amount of dye retained by the adsorbent strongly relates with the initial pH-level of the dye solution. For instance, the removal efficiency of investigated cationic dyes (MB and MG) rises with the elevation of the pH value in the dye solution. The maximum removal of MG and MB were 63.27, and 99.07 %, respectively at pH = 9. However, the inverse trend was observed for CR, where the maximum elimination (96.22 %) was obtained at pH = 1. In order to elucidate the impact of pH on dye removal, the point of zero charge (PZC) was determined. Fig. 1f shows that the surface of adsorbent is inert at pH 5.77. Further, the pH dependence of dye adsorption occurs due to the protonation of the adsorbent surface and electrostatic interactions between adsorbent and adsorbate molecules. Under the PZC (pH < pH_{PZC} = 5.77), the adsorbent surface was positively charged which induce strong electrostatic attraction for the anionic dye (CR) and repulsion for cationic dyes (MG, MB). However, for the cases where pH > pH_{PZC} = 5.77 the adsorbent surface is negatively charged which induces a strong electrostatic attraction for cationic dyes (MB, MG) and a strong electrostatic repulsion for CR-adsorbent system. This fact explains high adsorption capacity of MB and MG at high pH values, and the high adsorption capacity of CR at low pH values.

3.2.5. Effect of ionic strength

In general, a textile wastewater contains diverse salt ions (such as nitrates, chlorides, sulphates, carbonates, hydrogen carbonates) with different concentrations. To this note, it's crucial to assess the effect of ionic forces on the adsorption process of an analyte on the surface of an adsorbent. In this study, MB, MG, and CR onto UiO-66-NH_2 and the concentrations of NaCl was changed from 0 to 1 mol L^{-1}. Fig. 6 (a-c) illustrates a marked decline in the adsorbed amount of the dyes onto UiO-66-NH_2 with gradually increasing concentrations of NaCl which is in aligns harmoniously with the research findings in literature [64,65]. The negative effect of salts on adsorption can be explained by the competition between salt ions and dyes molecules for the same active sites available on the surface of an adsorbent.

3.2.6. Temperature effect

Temperature of the adsorption medium is regarded as one of paramount factor for examining the adsorption capacity of an

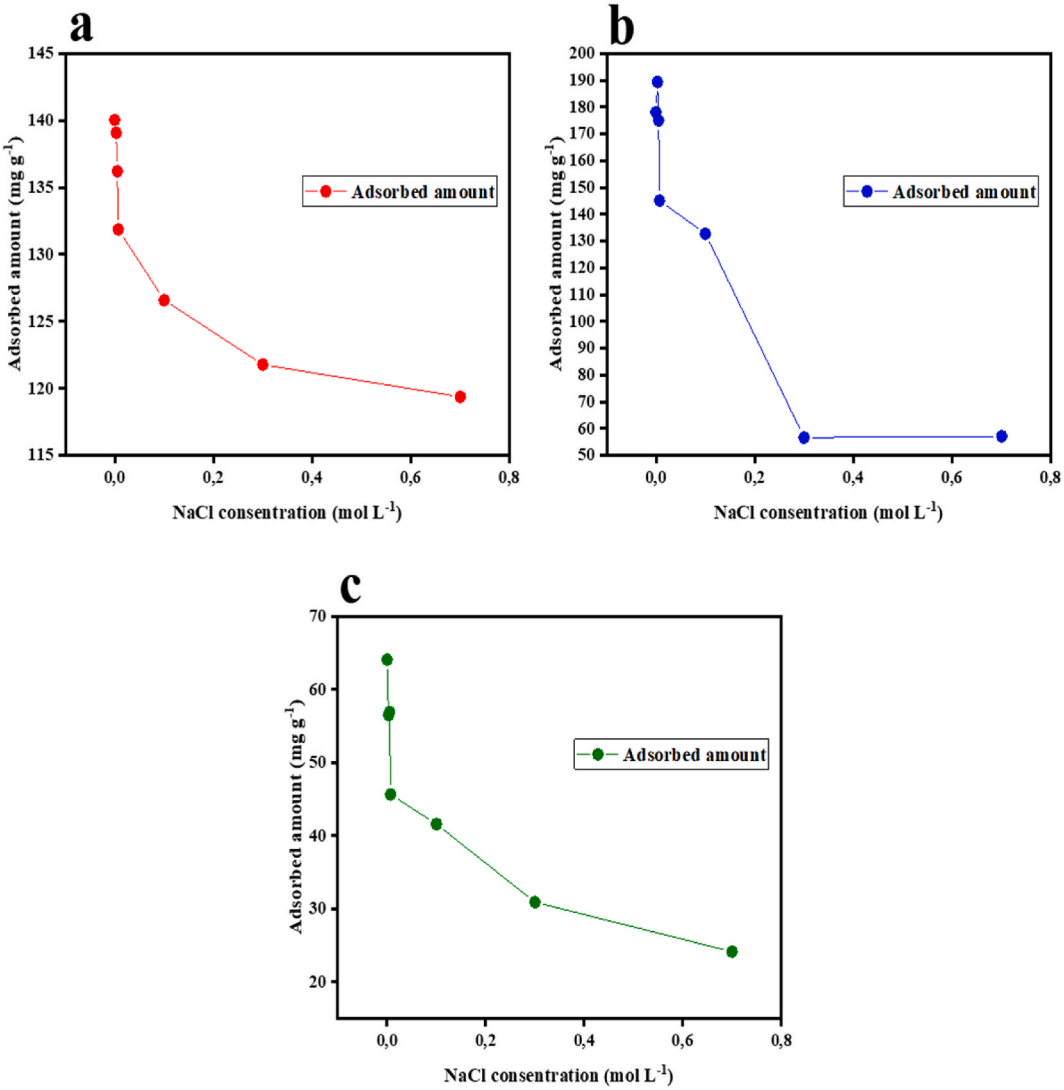

Fig. 6. Ionic strength effect on the removal of CR (a), MB (b), and MG (c).

adsorbent. A series of 4 experiments was carried out at varying temperatures (291.15, 303.15, 313.15 and 323.15 K) under optimized conditions (adsorbent dose, 5 mg, dye concentration, 10 mg L^{-1}, time to reach equilibrium, 60 min, and specific pH required for each investigated dye solution under ultrasound waves). Fig. 3S reveals that the dye adsorption rises significantly when the solution temperature increases from 291.15 to 323.15 K due to the reason that high temperature yields increased diffusion rate of adsorbate through the outer boundary layer of adsorbent particles by decreasing the viscosity of the solution [49,66].

3.3. Adsorption thermodynamics

To comprehensively analyze the thermodynamic characteristics linked with the adsorption of dye onto the UiO-66-NH_2 surface, the standard Gibbs free energy (ΔG°), the standard entropy change (ΔS°) and the standard enthalpy change (ΔH°) were determined using the following equations:

$$ln(k_d) = \frac{\Delta S^0}{R} - \frac{\Delta H^0}{RT} \tag{8}$$

$$k_d = \frac{Q_e}{c_e} \tag{9}$$

$$\Delta G^0 = \Delta H^0 - T\Delta S^0 \tag{10}$$

Q_e: adsorbed amount at equilibrium (mg g^{-1}), C_e: concentration of dye at equilibrium (mg L^{-1}), K_d: adsorption constant (L g^{-1}), T: the adsorption temperature (K), R: gas constant (8.314 J mol^{-1} K^{-1}).

According to results shown in Fig. 4S and Table 2, the values of ΔH° is positive indicating the endothermic nature of adsorption process whereas value of ΔG° is negative and decreases further with increase in temperature suggesting spontaneous adsorption process. The values of ΔS° are positive which means that disorder increases in the adsorbed phase. Further, these findings are consistent with the previous studies [67].

3.4. Adsorption isotherms

Adsorption isotherms have been determined by modeling the experimental data presented in Fig. 5S and Table 3 by following Langmuir and Freundlich models (equations (5)–(7)). From the values of coefficient of correlation, Langmuir model appears more suitable to elucidate the adsorption process of the target dyes onto UiO-66-NH_2. Therefore, the adsorption was favorable (separation factor $R_L < 1$ for the three dyes) and the dyes were adsorbed onto the adsorbent surfaces homogenously. The maximum adsorbed amount for the studied organic dyes was found to be $Q_m = 623$ mg g^{-1} (CR), 938. mg g^{-1} (MB), and 587 mg g^{-1} (MG). The results in Table 3 indicates that UiO-66-NH_2 exhibits high affinity to adsorb MB, CR, and MG. The quite high value of Langmuir constant (K_L) for MB compered to CR and MG indicates the high affinity of the adsorbent toward MB, which may be explained by the presence of two free tertiary amine groups and positive charge on S atom in the MB structure yielding a vigorous interaction between MB and the surface of UiO-66-NH_2. In addition, the minimum volume occupation by MB molecule ensured a minimal steric hindrance effect (MB volume occupation is less than MG and CR, respectively).

3.5. Kinetics study

In order to gain a more profound understand the adsorption process of MB, MG, and CR onto UiO-66-NH_2 surface, the experimental adsorption data were assessed utilizing both the non-linear PFO and PSO models. For the PSO model, the correlation coefficient value (R^2) was close to unity than that for PFO model as given in Fig. 6S and Table 4. This situation suggests that the adsorption kinetics of the dyes onto UiO-66-NH_2 follows a PSO process signifying that the adsorption of MB, MG, and CR onto UiO-66-NH_2 surface is of chemisorption nature.

3.6. Effect of ultrasound

Ultrasound, as an emerging technology in the realm of adsorption, has demonstrated its efficacy in the elimination of various substances (e.g., metal ions, anthocyanins, flavonoids, polyphenols, and organic pollutants [68]. This is attributed to its reduced reliance on organic solvents and sorbents, lower maintenance costs and energy consumption, simplicity, cost-effectiveness, and environmentally friendly characteristics [69]. To explore the effect of ultrasound waves for the adsorption of dye onto the adsorbent surface, two experiments were executed. In the first experiment adsorption process of dyes on adsorbent surface was studied under ultrasound waves and optimized experimental parameters. Whereas, the second adsorption experiment was conducted under the same optimized conditions but in the absence of ultrasound waves. The findings illustrated in Fig. 7 (a-c) indicates that the ultrasound waves enhanced the adsorption process by more than 200 % (Qe: 95 mg g^{-1} →240 mg g^{-1} for CR, Qe: 103 mg g^{-1} → 302 mg g^{-1} for MB and Qe: 124 mg g^{-1} →340 mg g^{-1} for MG), and decreased the necessary time to achieve the adsorption equilibrium for all three dyes (90 min → 60 min). This situation can be ascribed to the fact that ultrasound waves have the capability to induce acoustic cavitation, leading to the disruption of the solid matrix's surface of the adsorbent [70]. This phenomenon significantly enhances the rate of mass transfer of molecules from the solution to the adsorbents, resulting in a rapid increase in adsorption rates and a shorter time to reach equilibrium [71].

3.7. Adsorption mechanism prediction

In order to explain adsorption mechanism of dyes onto the surface of UiO-66-NH_2, the nature of functional groups on the surface of the UiO-66-NH_2 were examined using FTIR before and after adsorption of each dye (Fig. 8). From Fig. 8, it is evident that after dyes adsorption onto UiO-66-NH_2 surface, the FTIR spectrum shows some changes relative to the FTIR spectrum before adsorption. These changes are caused due to dyes adsorption (CR, MB, and MG molecules) on the surface of the adsorbent. However, FTIR analysis alone did not suffice to make comprehensive predictions regarding various types of interactions occurring within this adsorption phenomenon. Consequently, we supplemented our findings with an examination of the pH influence and the point of zero charge.

Table 2
Thermodynamic parameters of adsorption process.

Adsorbent	Dye	ΔH° (KJ mol^{-1})	ΔS° (J mol K^{-1})	ΔG° (KJ mol^{-1})				
				291.15 K	303.15 K	313.15 K	323.15 K	R^2
UiO-66-NH_2	**CR**	17.94	70.42	−2.5601	−3.4051	−4.1093	−4.8135	0.9458
	MB	16.59	69.16	−3.5388	−4.3687	−5.0603	−5.7519	0.9985
	MG	25.45	91.81	−1.28014	−2.3818	−3.2999	−4.2180	0.9787

Table 3
Parameters of adsorption isotherm models.

Dye	Langmuir model		Freundlich model	
CR	$\mathbf{Q_m^{-1}}$ (mg g	623	-	–
	$\mathbf{K_L^{-1}}$ (L mg	0.0338	**1/n**	0.3766
	$\mathbf{R_L}$	0.7473	$\mathbf{K_F}$	81.1371
	$\mathbf{R^2}$	0.9677	$\mathbf{R^2}$	0.8824
MB	$\mathbf{Q_m^{-1}}$ (mg g	938	-	–
	$\mathbf{K_L^{-1}}$ (L mg	0.0631	**1/n**	0.3216
	$\mathbf{R_L}$	0.6130	$\mathbf{K_F}$	180.3423
	$\mathbf{R^2}$	0.9514	$\mathbf{R^2}$	0.8360
MG	$\mathbf{Q_m^{-1}}$ (mg g	587	-	–
	$\mathbf{K_L^{-1}}$ (L mg	0.0337	**1/n**	0.3848
	$\mathbf{R_L}$	0.7477	$\mathbf{K_F}$	73.7318
	$\mathbf{R^2}$	0.9736	$\mathbf{R^2}$	0.9104

Table 4
Non-linear regression kinetic model factors for the adsorptive removal of CR, MB, and MG.

PFO					PSO		
Dye	$Q_{e\cdot exp}$ (mg g^{-1})	$Q_{e\cdot cal}$ (mg g^{-1})	K_1 ($Lmin^{-1}$)	R^2	$Q_{e\cdot cal}$ (mg g^{-1})	K_2 (g mg^{-1} min^{-1})	R^2
CR	133	138	0.0236	0.99385	136	0.0001	0.9957
MB	193	185	0.1142	0.99019	198	0.0008	0.9954
MG	64	59	0.0894	0.89318	64	0.0019	0.95171

In case of CR dye adsorption (Fig. 8a), after adsorption, a new peak was observed around 1023 cm^{-1} corresponding to SO_3^- in CR which confirms its enhanced adsorption. The peak at 1625 cm^{-1} corresponding to C═O stretching (O–C═O) from 2-amino-terephthalic acid is disappeared completely which may be attributed to the formation of hydrogen bonds between CR and the oxygen atom of C═O from UiO-66-NH_2 [72]. Additionally, the two peaks at 3391.7, and 3279.9 cm^{-1} corresponding to N–H vibration become broader indicting the strong hydrogen bonding connection between the CR and the –NH_2 group from UiO-66-NH_2 composite. The peak at 1542.4 cm^{-1} corresponding to C═C from aromatic rings is weakened which indicting the π-π staking between the aromatic rings of adsorbent and CR.

In case of MB adsorption (Fig. 8b), the peak at 1625.7 cm^{-1} disappeared completely which indicates the formation of hydrogen bond between MB and the oxygen atom of C═O from UiO-66-NH_2. The peaks at 3391.7, 3279.9 cm^{-1} became broader which indicate the formation of strong hydrogen bonding between the CR and the –NH_2 group from UiO-66-NH_2. The peak at 1542.4 cm^{-1} was weakened probably due to the π-π staking interaction between the aromatic rings from MB and the adsorbent, and electrostatic interactions between MB and UiO-66-NH_2.

For MG (Fig. 8c), in one hand the peak at 1625.7 cm^{-1} corresponding to C═O stretching from UiO-66-NH_2 is weakened along with the mild broadening of two peaks at 3391.7 and 3279.9 cm^{-1} corresponding to N–H vibration indicating the formation of hydrogen bond between MG and UiO-66-NH_2. However, the magnitude of hydrogen bond formed during the adsorption of malachite green is less than that of CR and MB as MG structure (tertiary amine) contains only one amino group that can form hydrogen bond. Additionally, the peak at 1542.4 was significantly weakened which indicates the existence of π-π staking between the aromatic rings of adsorbent and MG. In addition, a new peak appeared at 1148 cm^{-1} was ascribed to the tertiary amine group of MG.

The effect of pH and the point of zero charge can be used to understand more about the adsorption mechanism by considering tow cases. The first case is under the PZC (pH < 5.77) where the positively charged surface of UiO-66-NH_2 is (-NH_2 + H^+ → –NH_3^+ and C═O + H^+ → C═HO^+), causes more electrostatic attraction with the anionic dyes and more repulsion with the cationic dyes. This situation explains the enhanced adsorption capacity of CR and the weak adsorption capacity of MB and MG at low pH values. The second case is over the PZC (pH > 5.77) where the negatively charged surface of UiO-66-NH_2 (-NH_2 + OH^- → -NH^- + H_2O) exhibit enhanced electrostatic attraction with the cationic dyes and more repulsion with anionic ones. This situation explains the ultrahigh adsorption capacity of MB and MG and the weak adsorption capacity of CR at high pH values. Fig. 9 represents the schematic of the suggested adsorption mechanism for CR, MB, and MG onto UiO-66-NH_2 nanocompsites using ultrasound as an assisting technique.

3.8. Regeneration studies

Vitality and cost effectivity of a typical adsorption process is governed by the stability of an adsorbent in adsorption cycles. In this experiment the regenerability of UiO-66-NH_2 was achieved by washing the adsorbent several time with $CHCl_3$. Then the regenerated adsorbent was subjected to adsorption test for CR, MB, and MG separately and the findings are tabulated in Table 5. The adsorption capability remained unchanged after the first regeneration, then dye elimination gradually decreased from 90.0, 91.0, and 88.1 % for CR, MB, and MG, respectively. These results illustrated the possibility of employing the UiO-66-NH_2 to adsorb the target dyes repeatedly without significant loss in its retention capability.

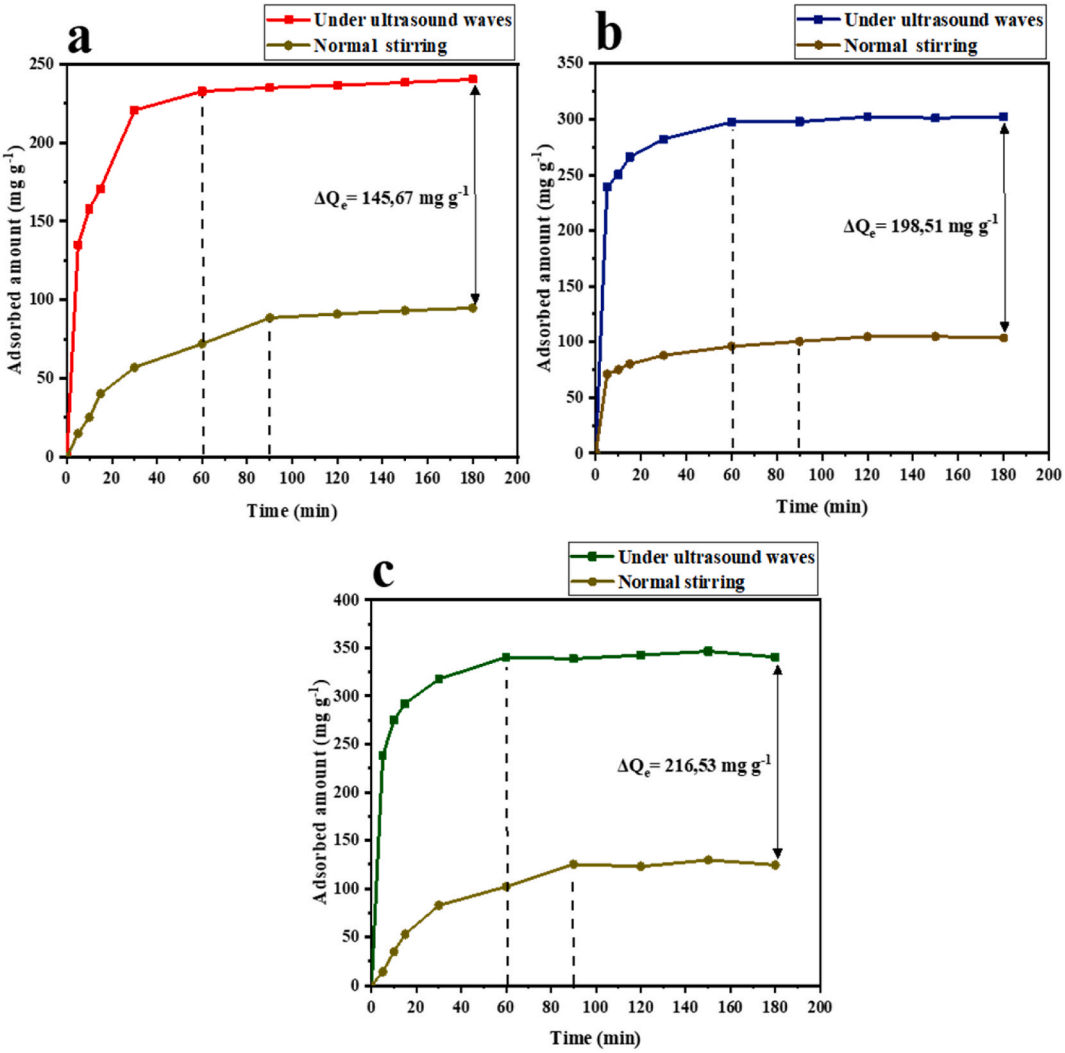

Fig. 7. The effect of ultrasound waves in adsorption of CR (a), MB (b), and MG (c) for concentration of 30 mg L^{-1}.

3.9. Comparison of adsorption capacity of UiO-66-NH_2-assisted ultrasound with other MOFs adsorbents

A comparison of a maximum adsorbed amount for MG, CR, and MB dyes using different MOFs as adsorbents is given in Table 6 [46,47,67,73–76], which illustrates that ultrasonication-assisted UiO-66-NH_2 exhibits better adsorption efficiency for target dyes relative to other adsorbents. Moreover, through a comparative examination of the outcomes from the study employing UiO-66-NH_2 for CR elimination in water samples [46], UiO-66-NH_2 assisted with ultrasound (our own findings) for CR removal exhibited extremely high adsorption capacity (623 mg g^{-1}) (Table 6). This examination compellingly underscores the substantial advantages conferred by ultrasound as an assisting technique within the domain of adsorption studies. Resultantly, ultrasonication-assisted UiO-66-NH_2 can be considered as a prospective candidate for the removal of MB, CR, and MG dyes from aqueous solutions.

4. Applications in different water samples

The adsorption of CR, MG, and MB in water (wastewater, dam water, and river water) was executed out to assess the efficacy of UiO-66-NH_2 in actual industrial applications. In the adsorption experiments, 5 mg of UiO-66-NH_2 was introduced into 100 mL of dye solution containing 30 mg L^{-1} of dye concentration under ultrasound waves for contact time of 60 min. Fig. 10 (a-c) shows the difference in adsorbed amount of target dye between the synthetic solution (distilled water containing dye) and the three real solutions. From the results a progressive decrease in adsorbed amount of dye is evident as in dam solution, river solution, and wastewater solution, respectively which can be ascribed to high concentration levels of different salts in the respective water sources which is in accord with the results found in ionic strength study (Fig. 2S). The findings indicate that, for the removal of CR (Qe = 248.3 mg g^{-1} in the synthetic solution), our adsorbent lost its efficacy by 13.7 % (Qe = 214.3 mg g^{-1}) in dam water, 19.2 % (Qe = 200.5 mg g^{-1}) in

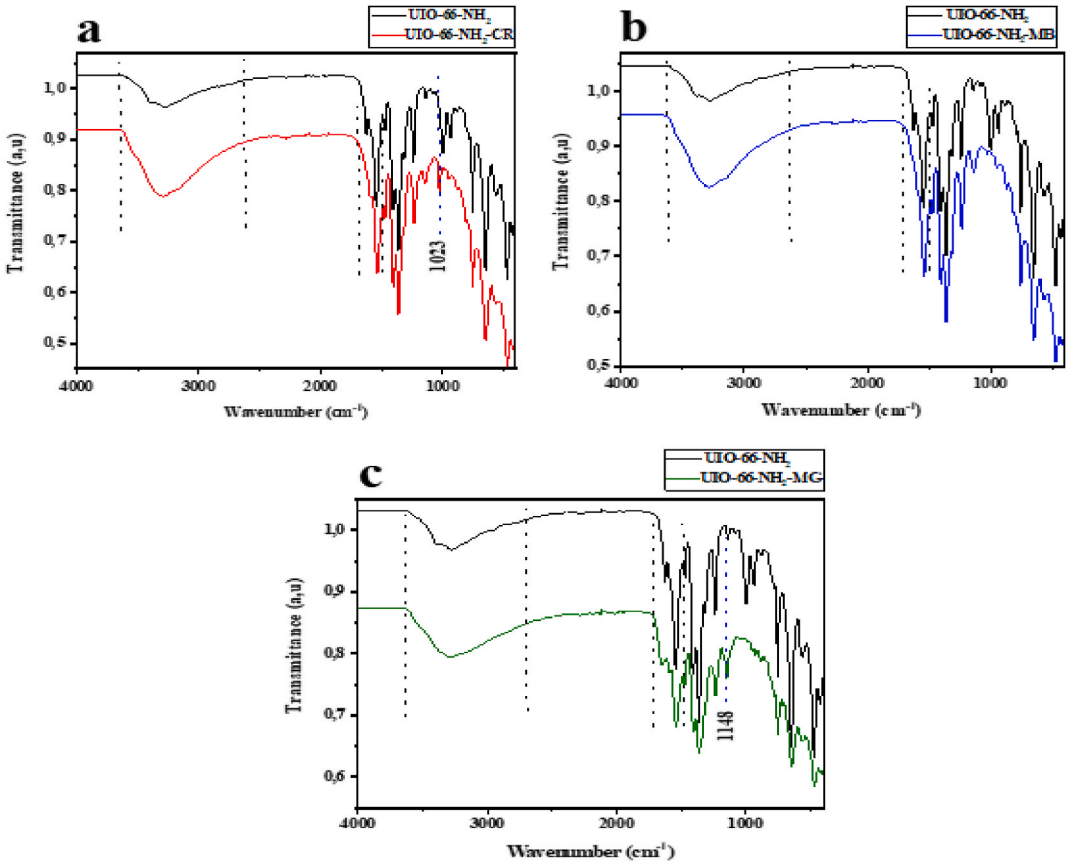

Fig. 8. FTIR comparison of functionalities present on UiO-66-NH_2 surface prior and after adsorption of CR (a), MB (b), and MG (c).

river water, and 38.9 % (Qe = 151.8 mg g^{-1}) in wastewater. For MB (Qe = 312.0 mg g^{-1} in the synthetic solution), our adsorbent lost its efficacy by 23.1 % (Qe = 240.0 mg g^{-1}) in dam water, 30.7 % (Qe = 216.1 mg g^{-1}) in river water, and 41.2 % (Qe = 183.5 mg g^{-1}) in wastewater. For MG (Qe = 348.0 mg g^{-1} in the synthetic solution), our adsorbent lost its efficacy by 28.8 % (Qe = 247.8 mg g^{-1}) in dam water, 38.6 % (Qe = 213.7 mg g^{-1}) in river water, and 51.6 % (Qe = 168.4 mg g^{-1}) in wastewater. Undoubtedly, the adsorbent experiences a certain percentage loss in its efficacy from dam water to wastewater, it still exhibits a significant adsorption capacity across various types of water samples which supports its potential for practical applications.

5. Conclusion

In the current study, we prepared UiO-66-NH_2 and studied its application with ultrasound for remediation of anionic (CR) and cationic (MB and MG) dye pollutants from real water samples. The experimental determinants such as organic dye concentration, contact duration, temperature, ionic strength, and pH had a substantial influence on the remediation of organic dye pollutants from their water-based matrix. The results showcased that dyes removal from aqueous solution accorded well with the Langmuir isotherm model which means that the pollutants constructed a monolayer on the surface of adsorbent. The research findings confirmed that the adsorption process undergoes a PSO kinetic model implying a strong interaction between adsorbent and pollutant (chemisorption), which suggests that the adsorbent is less susceptible to subjected to facile desorption processes under various conditions encountered in real-world environments beyond the laboratory. Additionally, the findings confirm that the use of ultrasonication in contrast to conventional stirring methods was found to result in an exceptional improvement in dyes removal by enhancing the adsorption capacity and reduction of time needed to eliminate the pollutants. This enhancement was attributed to various factors, such as the increase in interfacial area, solvent penetration, and anti-aggregation effect, which ultimately enhanced the interactions between the adsorbent material and the adsorbate molecules. All of these aspects substantially enhance the commercial viability of the adsorbent, rendering it highly promising for large-scale applications in real world samples. UiO-66-NH_2 was also tested for its suitability to remove CR, MG, and MB from real wastewater, river, and dam water samples, and even under seemingly optimal conditions found in synthetic water, it still displayed a high adsorption capacity. From these results, it was inferred that the use of UiO-66-NH_2 as an adsorbent under ultrasound waves exhibit good potential to be employed in practical real-world applications.

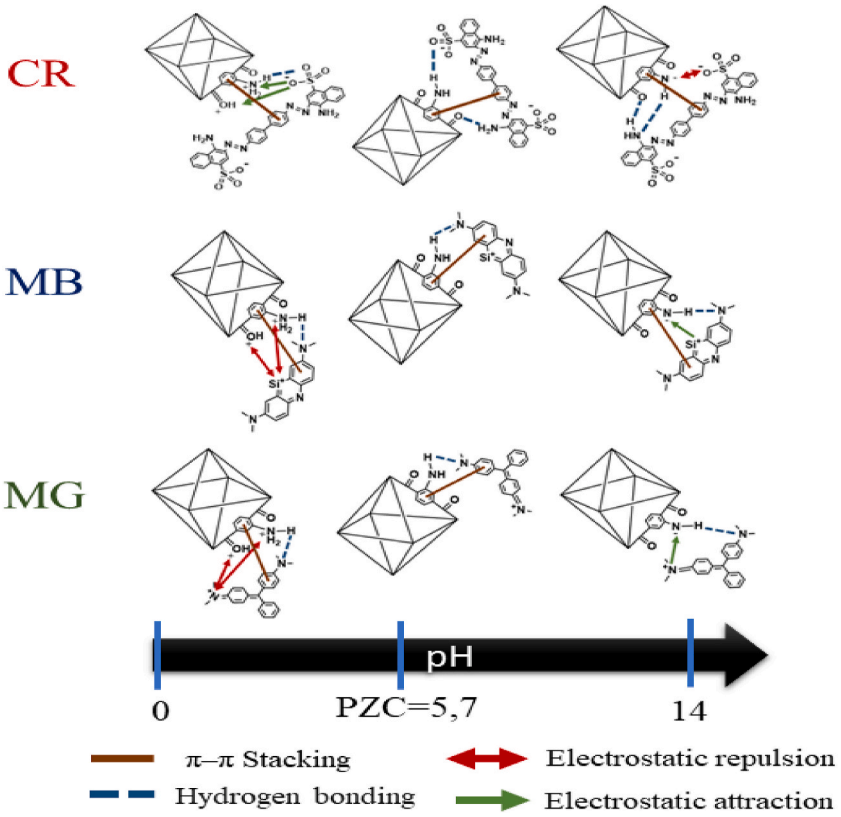

Fig. 9. Schematic of the suggested adsorption mechanism for CR, MB, and MG onto UiO-66-NH_2.

Table 5
The adsorbed amount of CR, MB, and MG onto UiO-66-NH_2 in different cycles.

Dye	Cycle 1	Cycle 2	Cycle 3	Cycle 4
	Efficiency (%)			
CR	96.3	93.3	92.5	90.0
MB	96.4	93.3	92.7	91.0
MG	95.2	92.1	88.9	88.1

Table 6
Comparative performance of UiO-66-NH_2 with other adsorbent in literature in terms of adsorption capacity.

MOF	Surface area (m^2 g^{-1})	Target	Adsorption capacity (mg g^{-1})	Mechanism	Reference
UiO-66	1276	MG MB	133 370	Hydrogen bonding, π-π stacking interaction, physical adsorption, and electrostatic interaction	[47]
Ce(III)-doped UiO-67	1911	MB	398.9	Electrostatic and π–π interactions	[73]
TFMOF	89.9	CR	252.3	Electrostatic interactions	[67]
WPU-SS-MOF	341	CR MB	76.6 27.8	Hydrogen bonding, π-π stacking interaction Electrostatic interactions	[76]
MIL-121	3.1	CR MB	69.7 27.8	H-bonding Electrostatic interactions	[75]
Fe-MOF	1858	CR MB	42.9 119	Hydrogen bonding π-π stacking interaction	[74]
UiO-66-NH_2	–	CR	94.2	Hydrogen bonding π-π stacking interaction electrostatic interaction Lewis acid-base interaction	[46]
UiO-66-NH_2 assisted with US	679	CR MB MG	623 938 587	Hydrogen bonding π-π stacking interaction electrostatic interaction	This work

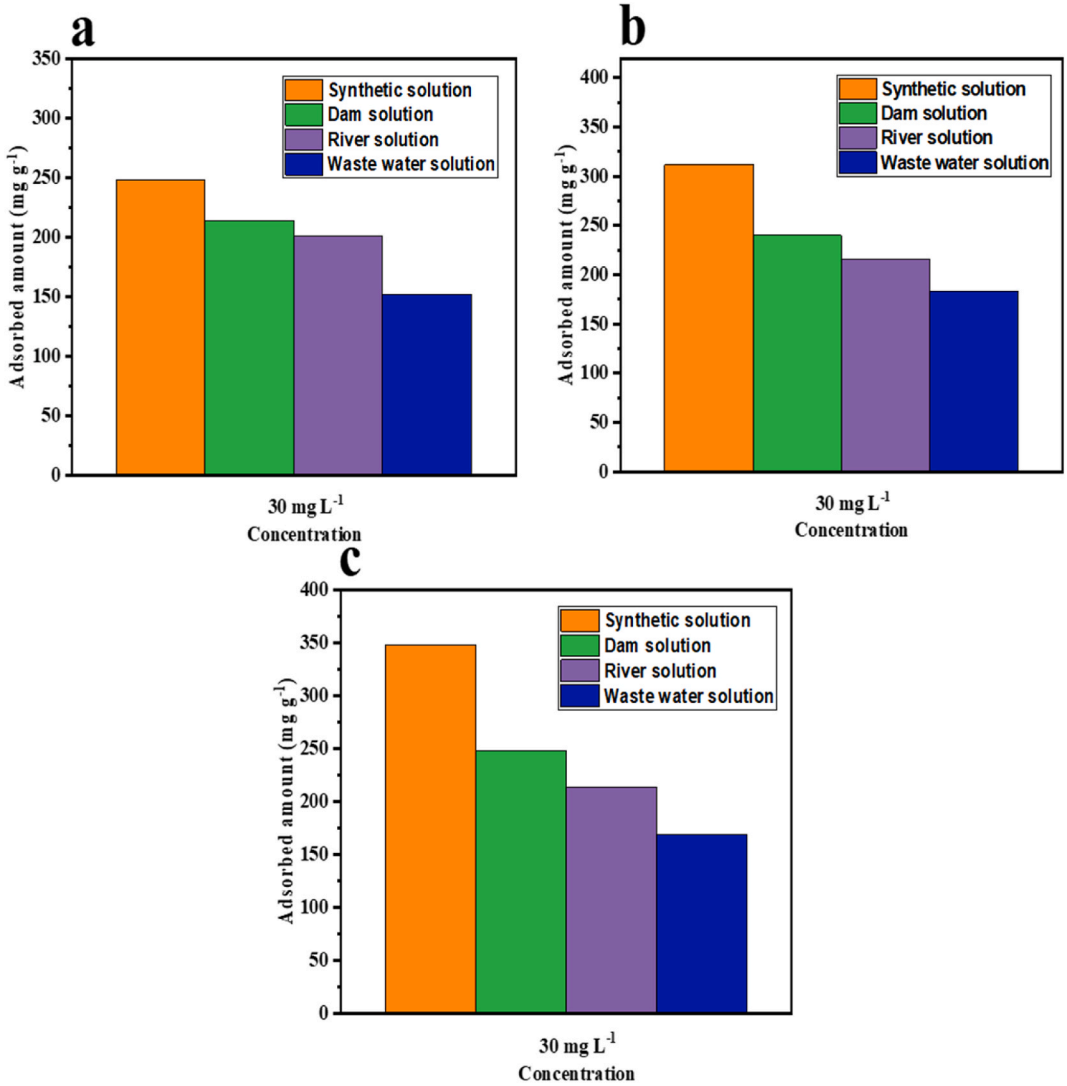

Fig. 10. Comparison of adsorbed amount CR (a), MB (b), and MG (c) in synthetic solution and real water samples (e.g., dam, river, and wastewater).

Data availability statement

All the data related to our study is already included in article/supplementary material/referenced in article. Furthermore, the data associated with our study has not been deposited into a publicly available repository.

CRediT authorship contribution statement

Abdeslam Assafi: Formal analysis, Investigation, Methodology, Validation, Conceptualization, Writing – original draft. **Youssef Aoulad El Hadj Ali:** Data curation, Investigation, Software, Visualization. **Rasmiah S. Almufarij:** Funding acquisition, Investigation, Resources. **Lamia Hejji:** Data curation, Methodology, Resources. **Nadeem Raza:** Investigation, Project administration, Supervision, Validation, Writing – review & editing. **Luis Pérez Villarejo:** Data curation, Methodology, Resources, Visualization. **Badredine Souhail:** Formal analysis. **Abdelmonaim Azzouz:** Formal analysis, Investigation, Resources, Supervision, Writing – original draft, Writing – review & editing. **Ehab A. Abdelrahman:** Software, Visualization.

Declaration of competing interest

The authors declare that they have no known competing financial interests or personal relationships that could have appeared to influence the work reported in this paper.

Acknowledgements

The authors acknowledge the support from Deanship at Scientific Research, Imam Mohammad Ibn Saud Islamic University (IMSIU), Riyadh 11623, Saudi Arabia. Rasmiah S. Almufarij would like to thank Princess Nourah bint Abdulrahman University Researchers Supporting Project number (PNURSP2023R316), Princess Nourah bint Abdulrahman University, Riyadh, Saudi Arabia. E.R. C. thanks to project TED2021-130756B–C31 funded by MCIN/AEI/10.13039/501100011033 and by "ERDF A way of making Europe" by the European Union Next Generation EU/PRTR.

Appendix A. Supplementary data

Supplementary data to this article can be found online at https://doi.org/10.1016/j.heliyon.2023.e22001.

References

[1] A. Wutich, et al., Measuring human water needs, Am. J. Hum. Biol. 32 (1) (2020), e23350.
[2] S. Sarkar, et al., Green polymeric nanomaterials for the photocatalytic degradation of dyes: a review, Environ. Chem. Lett. 18 (2020) 1569–1580.
[3] A. Modwi, et al., Superior removal of dyes by mesoporous MgO/g-C3N4 fabricated through ultrasound method: adsorption mechanism and process modeling, Environ. Res. 205 (2022), 112543.
[4] M. Wang, et al., Simultaneously enhanced treatment efficiency of simulated hypersaline azo dye wastewater and membrane antifouling by a novel static magnetic field membrane bioreactor (SMFMBR), Sci. Total Environ. 821 (2022), 153452.
[5] C. Lu, et al., A highly efficient technique to simultaneously remove acidic and basic dyes using magnetic ion-exchange microbeads, J. Environ. Manag. 304 (2022), 114173.
[6] R.K. Gautam, I. Tiwari, Humic acid functionalized magnetic nanomaterials for remediation of dye wastewater under ultrasonication: application in real water samples, recycling and reuse of nanosorbents, Chemosphere 245 (2020), 125553.
[7] E. Valadez-Renteria, J. Oliva, V. Rodriguez-Gonzalez, Photocatalytic materials immobilized on recycled supports and their role in the degradation of water contaminants: a timely review, Sci. Total Environ. 807 (2022), 150820.
[8] S.A. Haladu, Highly efficient adsorption of malachite green dye onto a cross-linked pH-responsive cycloterpolymer resin: kinetic, equilibrium and thermodynamic studies, J. Mol. Liq. 357 (2022), 119115.
[9] A.S. Eltaweil, et al., Mesoporous magnetic biochar composite for enhanced adsorption of malachite green dye: characterization, adsorption kinetics, thermodynamics and isotherms, Adv. Powder Technol. 31 (3) (2020) 1253–1263.
[10] A.S. Eltaweil, et al., Graphene oxide incorporated cellulose acetate beads for efficient removal of methylene blue dye; isotherms, kinetic, mechanism and co-existing ions studies, J. Porous Mater. 30 (2) (2023) 607–618.
[11] E. Eze, et al., Efficient Removal of Noxious Methylene Dye by Low-Cost and Reusable Composite Beads Based on Cellulose Acetate/banana Pseudo-stem Fiber, Biomass Conversion and Biorefinery, 2023.
[12] X. Wang, et al., Adsorption of methylene blue and Congo red from aqueous solution on 3D MXene/carbon foam hybrid aerogels: a study by experimental and statistical physics modeling, J. Environ. Chem. Eng. 11 (1) (2023), 109206.
[13] A.S. Eltaweil, et al., Magnetic hierarchical flower-like Fe3O4@ZIF-67/CuNiMn-LDH catalyst with enhanced redox cycle for Fenton-like degradation of Congo red: optimization and mechanism, Environ. Sci. Pollut. Control Ser. 30 (30) (2023) 75332–75348.
[14] L. Liu, et al., Treatment of industrial dye wastewater and pharmaceutical residue wastewater by advanced oxidation processes and its combination with nanocatalysts: a review, J. Water Proc. Eng. 42 (2021), 102122.
[15] G.A. Ismail, H. Sakai, Review on effect of different type of dyes on advanced oxidation processes (AOPs) for textile color removal, Chemosphere (2021), 132906.
[16] N. Raza, et al., ZnO–ZnTe hierarchical superstructures as solar-light-activated photocatalysts for azo dye removal, Environ. Res. 194 (2021), 110499.
[17] N. Raza, et al., Solar-light-active silver phosphate/titanium dioxide/silica heterostructures for photocatalytic removal of organic dye, J. Clean. Prod. 254 (2020), 120031.
[18] N. Abbas, et al., The photocatalytic performance and structural characteristics of nickel cobalt ferrite nanocomposites after doping with bismuth, J. Colloid Interface Sci. 594 (2021) 902–913.
[19] H. Agbe, et al., H2O2 rejuvenation-mediated synthesis of stable mixed-morphology Ag3PO4 photocatalysts, Heliyon 4 (4) (2018).
[20] M. Taheri, Techno-economical aspects of electrocoagulation optimization in three acid azo dyes' removal comparison, Cleaner Chemical Engineering 2 (2022), 100007.
[21] Z. Bencheqroun, et al., Fe (III)-exchanged zeolites as efficient electrocatalysts for Fenton-like oxidation of dyes in aqueous phase, J. Environ. Chem. Eng. 10 (3) (2022), 107891.
[22] X. Guo, et al., Flower-like FeMoO4@ 1T-MoS2 micro-sphere for effectively cleaning binary dyes via photo-Fenton oxidation, J. Colloid Interface Sci. 622 (2022) 284–297.
[23] D. Han, et al., Critical review of electro-kinetic remediation of contaminated soils and sediments: mechanisms, performances and technologies, Water, Air, Soil Pollut. 232 (8) (2021) 335.
[24] A.A. Prakash, et al., Bio-electrokinetic remediation of crude oil contaminated soil enhanced by bacterial biosurfactant, J. Hazard Mater. 405 (2021), 124061.
[25] Y.W. Berkessa, et al., Treatment of anthraquinone dye textile wastewater using anaerobic dynamic membrane bioreactor: performance and microbial dynamics, Chemosphere 238 (2020), 124539.
[26] R. Li, et al., Aquatic environment remediation by atomic layer deposition-based multi-functional materials: a review, J. Hazard Mater. 402 (2021), 123513.
[27] T. Krithiga, et al., Persistent Organic Pollutants in Water Resources: Fate, Occurrence, Characterization and Risk Analysis, Science of The Total Environment, 2022, 154808.
[28] A. Karmakar, et al., Highly efficient adsorptive removal of organic dyes from aqueous solutions using polyaromatic group-containing Zn (II)-Based coordination polymers, Cryst. Growth Des. 22 (4) (2022) 2248–2265.
[29] M. Zheng, et al., MOFs and GO-based composites as deliberated materials for the adsorption of various water contaminants, Separ. Purif. Technol. (2022), 121187.
[30] F. Subhan, et al., Adsorption and reusability performance of hierarchically porous silica (MMZ) for the removal of MB dye from water, Inorg. Chem. Commun. 139 (2022), 109380.
[31] M. Kasula, et al., Silver metal organic frameworks and copper metal organic frameworks immobilized on graphene oxide for enhanced adsorption in water treatment, Chem. Eng. J. 439 (2022), 135542.
[32] D. Mukherjee, et al., Hierarchical graphite oxide decorated UiO-66 for ultrahigh adsorption of dye with synergistic effect of ultrasonication: experimental and density functional theory study, Separ. Purif. Technol. 294 (2022), 121217.

[33] E.A. Abdelrahman, et al., Facile synthesis and characterization of novel nanostructures for the efficient disposal of crystal violet dye from aqueous media, Inorganics 11 (8) (2023) 339.
[34] M.A. El-Nemr, M.A. Hassaan, I. Ashour, Fabrication of N-doping activated carbons from fish waste and sawdust for Acid Yellow 36 dye removal from an aquatic environment, Sci. Rep. 13 (1) (2023) 5892.
[35] G. Mujtaba, et al., Simultaneous adsorption of methylene blue and amoxicillin by starch-impregnated MgAl layered double hydroxide: parametric optimization, isothermal studies and thermo-kinetic analysis, Environ. Res. 235 (2023), 116610.
[36] L.R. Rad, M. Anbia, Zeolite-based composites for the adsorption of toxic matters from water: a review, J. Environ. Chem. Eng. 9 (5) (2021), 106088.
[37] N.C. Joshi, P. Gururani, Advances of graphene oxide based nanocomposite materials in the treatment of wastewater containing heavy metal ions and dyes, Current Research in Green and Sustainable Chemistry (2022), 100306.
[38] G. Cai, et al., Metal–organic framework-based hierarchically porous materials: synthesis and applications, Chem. Rev. 121 (20) (2021) 12278–12326.
[39] E. Moumen, L. Bazzi, S. El Hankari, Metal-organic frameworks and their composites for the adsorption and sensing of phosphate, Coord. Chem. Rev. 455 (2022), 214376.
[40] Y. Feng, et al., Fast adsorption of methyl blue on zeolitic imidazolate framework-8 and its adsorption mechanism, RSC Adv. 6 (111) (2016) 109608–109612.
[41] M.J. Uddin, R.E. Ampiaw, W. Lee, Adsorptive removal of dyes from wastewater using a metal-organic framework: a review, Chemosphere 284 (2021), 131314.
[42] J. Abdi, et al., Synthesis of metal-organic framework hybrid nanocomposites based on GO and CNT with high adsorption capacity for dye removal, Chem. Eng. J. 326 (2017) 1145–1158.
[43] F.h. Wei, et al., Synthesis of graphene oxide/metal-organic frameworks composite materials for removal of Congo red from wastewater, ChemistrySelect 4 (19) (2019) 5755–5762.
[44] S. Luo, J. Wang, MOF/graphene oxide composite as an efficient adsorbent for the removal of organic dyes from aqueous solution, Environ. Sci. Pollut. Control Ser. 25 (6) (2018) 5521–5528.
[45] R.M. Rego, M.D. Kurkuri, M. Kigga, A comprehensive review on water remediation using UiO-66 MOFs and their derivatives, Chemosphere (2022), 134845.
[46] Y. Lei, et al., Enhanced adsorption of dyes by functionalized UiO-66 nanoparticles: adsorption properties and mechanisms, J. Mol. Struct. 1292 (2023), 136111.
[47] F. Ahmadijokani, et al., Superior chemical stability of UiO-66 metal-organic frameworks (MOFs) for selective dye adsorption, Chem. Eng. J. 399 (2020), 125346.
[48] K. Vikrant, et al., Application of Zr-cluster-based MOFs for the adsorptive removal of aliphatic aldehydes (C1 to C5) from an industrial solvent, ACS Appl. Mater. Interfaces 11 (47) (2019) 44270–44281.
[49] Y. Aoulad El Hadj Ali, et al., Dried sewage sludge as an efficient adsorbent for pollutants: cationic methylene blue removal case study, Nanotechnology for Environmental Engineering 6 (1) (2021).
[50] V. Krstić, Chapter 14 - role of zeolite adsorbent in water treatment, in: B. Bhanvase, et al. (Eds.), Handbook of Nanomaterials for Wastewater Treatment, Elsevier, 2021, pp. 417–481.
[51] M. Pooresmaeil, H. Namazi, Chapter 14 - application of polysaccharide-based hydrogels for water treatments, in: Y. Chen (Ed.), Hydrogels Based on Natural Polymers, Elsevier, 2020, pp. 411–455.
[52] Y. Aoulad El Hadj Ali, et al., From Disposal Problem to Valuable Product: the Route of Sewage Sludge as an Adsorbent for congo Red Removal, Biomass Conversion and Biorefinery, 2023, pp. 1–14.
[53] Y. Cao, et al., UiO-66-NH2/GO composite: synthesis, characterization and CO2 adsorption performance, Materials 11 (4) (2018) 589.
[54] S. Askari, M.M. Khodaei, M. Jafarzadeh, Heterogenized phosphinic acid on UiO-66-NH2: a bifunctional catalyst for the synthesis of polyhydroquinolines, Catal. Lett. 152 (5) (2022) 1517–1529.
[55] P. Tian, et al., Zr-MOFs based on Keggin-type polyoxometalates for photocatalytic hydrogen production, J. Mater. Sci. 53 (17) (2018) 12016–12029.
[56] X. Wang, et al., Microwave irradiation induced UIO-66-NH2 anchored on graphene with high activity for photocatalytic reduction of CO2, Appl. Catal. B Environ. 228 (2018) 47–53.
[57] X. Wang, et al., Synthesis of Au/UiO-66-NH2/Graphene composites as efficient visible-light photocatalysts to convert CO2, Int. J. Hydrogen Energy 46 (21) (2021) 11621–11635.
[58] H. Zeng, et al., A novel strategy for enhancing the performance of membranes for dyes separation: embedding PAA@ UiO-66-NH2 between graphene oxide sheets, Chem. Eng. J. 403 (2021), 126281.
[59] M. Zhang, et al., On-line enrichment and determination of aristolochic acid in medicinal plants using a MOF-based composite monolith as adsorbent, J. Chromatogr. B 1159 (2020), 122343.
[60] K.-Y.A. Lin, Y.-T. Liu, S.-Y. Chen, Adsorption of fluoride to UiO-66-NH2 in water: stability, kinetic, isotherm and thermodynamic studies, J. Colloid Interface Sci. 461 (2016) 79–87.
[61] X. Shi, et al., Effective toluene adsorption over defective UiO-66-NH2: an experimental and computational exploration, J. Mol. Liq. 316 (2020), 113812.
[62] L. Valenzano, et al., Disclosing the complex structure of UiO-66 metal organic framework: a synergic combination of experiment and theory, Chem. Mater. 23 (7) (2011) 1700–1718.
[63] S. Sawasdee, H. Jankerd, P. Watcharabundit, Adsorption of dyestuff in household-scale dyeing onto rice husk, Energy Proc. 138 (2017) 1159–1164.
[64] L. Mouni, et al., Removal of Methylene Blue from aqueous solutions by adsorption on Kaolin: kinetic and equilibrium studies, Appl. Clay Sci. 153 (2018) 38–45.
[65] J. Cheng, et al., Highly efficient removal of methylene blue dye from an aqueous solution using cellulose acetate nanofibrous membranes modified by polydopamine, ACS Omega 5 (10) (2020) 5389–5400.
[66] C. Djilani, et al., Adsorption of dyes on activated carbon prepared from apricot stones and commercial activated carbon, J. Taiwan Inst. Chem. Eng. 53 (2015) 112–121.
[67] J. Liu, H. Yu, L. Wang, Superior absorption capacity of tremella like ferrocene based metal-organic framework in removal of organic dye from water, J. Hazard Mater. 392 (2020), 122274.
[68] F. Lu, et al., Enhancement of ultrasound on the dynamic decolorization of wolfberry (Lycium barbarum) polysaccharides, LWT 145 (2021), 111384.
[69] B.B. Ismail, et al., Valorisation of baobab (Adansonia digitata) seeds by ultrasound assisted extraction of polyphenolics. Optimisation and comparison with conventional methods, Ultrason. Sonochem. 52 (2019) 257–267.
[70] B.B. Ismail, et al., Ultrasound-assisted adsorption/desorption for the enrichment and purification of flavonoids from baobab (Adansonia digitata) fruit pulp, Ultrason. Sonochem. 65 (2020), 104980.
[71] L. Tao, et al., Efficient decolorization of oligosaccharides in ginseng (Panax ginseng) residue using ultrasound-assisted macroporous resin, Food Chem. 419 (2023), 136098.
[72] A.S. Eltaweil, et al., Ultra-high adsorption capacity and selective removal of Congo red over aminated graphene oxide modified Mn-doped UiO-66 MOF, Powder Technol. 379 (2021) 407–416.
[73] J.-M. Yang, et al., Rapid adsorptive removal of cationic and anionic dyes from aqueous solution by a Ce (III)-doped Zr-based metal–organic framework, Microporous Mesoporous Mater. 292 (2020), 109764.
[74] H. Ghasempour, F. Zarekarizi, A. Morsali, Acyl amide-functionalized and water-stable iron-based MOF for rapid and selective dye removal, CrystEngComm 24 (22) (2022) 4074–4084.
[75] N. Hu, et al., Temperature-regulated formation of hierarchical pores and defective sites in MIL-121 for enhanced adsorption of cationic and anionic dyes, Separ. Purif. Technol. 314 (2023), 123650.
[76] H.-W. Li, et al., Construction of self-healable and recyclable waterborne polyurethane-MOF membrane for adsorption of dye wastewater based on solvent etching deposition method, Separ. Purif. Technol. 320 (2023), 124145.